Progress In Electromagnetics Research C, Vol. 128, 97–111, 2023

Design and Analysis of a Novel U-PM Vernier Machine with HTS Bulks

Zhangtao Kui, Libing Jing*, Zeyu Min, and Kun Yang

Abstract—In order to improve the electromagnetic performance of permanent magnet vernier machines (PMVMs) at a high pole ratio, a novel U-type permanent magnet (U-PM) vernier machine with high-temperature superconductor (HTS) bulks is proposed. HTS bulks are introduced between the stator modulating teeth, and alternating flux bridges and U-PMs are added in the rotor yoke. The structure can reduce the magnetic flux leakage, provide a magnetic circuit for the low pole pair working magnetic field, weaken the magnetic barrier effect, and improve the torque density of the machine. The parametric model of the proposed machine with 23 pole pairs of the rotor and 4 pole pairs of the stator is established by the finite element software. In addition, some key parameters of the proposed machine are layered by parameter sensitivity analysis, and then the machine is optimized by genetic algorithm. Compared with the conventional machine, the proposed machine increases the average electromagnetic torque by 69%, reduces the torque ripple to 1.7%, increases the power factor to 0.73, and increases the efficiency to 85.3%.

1. INTRODUCTION

With the continuous development of superconducting technology, the larger-scale application of superconducting machines is an inevitable trend under the severe situation of energy and environment [1]. It is well known that high-temperature superconducting (HTS) machines have been widely used in aircraft propulsion, wind power generation, ship propulsion, and other fields due to their advantages of low magnetic flux leakage, high power factor, and high efficiency [2]. However, for those low-speed applications, HTS machines often need to be combined with mechanical gearboxes to adjust speed, which inevitably leads to mechanical losses and efficiency degradation [3]. Therefore, the direct drive application of superconducting machines has great development potential in low-speed applications [4].

In recent years, permanent magnet vernier machine (PMVM) has attracted more and more attention in direct drive systems due to its excellent high torque and flux regulation characteristics at low speed [5]. However, compared with conventional permanent magnet machines, PMVM often has a lower power factor due to large magnetic flux leakage [6]. Spoke array permanent magnet vernier machine (SAPMVM) can reduce the magnetic flux leakage between permanent magnets and improve the power factor through the flux-focusing effect [7]. However, at a high pole ratio, the torque increase of the SAPMVM is not obvious due to the magnetic barrier effect. In [8], adding flux bridges to the rotor yoke can weaken the magnetic barrier effect and increase the electromagnetic torque. However, the introduction of the flux bridge will further increase the magnetic flux leakage and reduce the power factor [9].

In order to combine the advantages of PMVM and HTS machine to pursue higher torque density and machine efficiency, various PMVMs with HTS bulks have been proposed. HTS bulks can be used between

Received 7 November 2022, Accepted 20 December 2022, Scheduled 31 December 2022
* Corresponding author: Libing Jing (jinglibing@ctgu.edu.cn).
The authors are with the College of Electrical Engineering & New Energy, China Three Gorges University, Yichang 443002, China.

machine slots to shield the magnetic field, reduce magnetic leakage, and improve the electromagnetic performance of the machine [10]. In [11], a new HTS dual stator linear PMVM with a Halbach array is proposed, which can significantly improve the force transmission capacity and reduce magnetic flux leakage. By incorporating the HTS bulks into the machine, the magnetic flux modulation capability can be further improved [12]. However, due to the insertion of HTS bulks between the modulation teeth, the air gap structure is changed, resulting in a decrease in the sinusoidal back EMF or an increase in torque ripple [13]. To improve the electromagnetic performance of the machine, Taguchi method, response surface method (RSM), and genetic algorithm (GA) are usually used to analyze and optimize some key parameters of the machine [14–16].

In this paper, a novel U-PM vernier machine with HTS bulks is proposed, which can effectively weaken the magnetic barrier effect of the motor, improve the torque density, and improve the power factor. At the same time, the complex structure of the proposed machine makes it necessary to consider more structural parameters in the optimization analysis process. On the other hand, the design and analysis of the machine is a complex multi-dimensional optimization process. In this study, the electromagnetic torque, torque ripple, and power factor are taken as the optimization objectives, and the sensitivity of the machine parameters is layered. GA is used to analyze the key parameters, and finally, the optimal structural parameters of the machine are determined. The article is organized as follows. Section 2 gives the topology of the machine and introduces the working principle. In Section 3, the optimization method is formulated, and the machine parameters are determined. In Section 4, the electromagnetic performances of conventional SAPMVM and the proposed machine are compared by the finite element model. Finally, some conclusions are drawn in Section 5.

2. STRUCTURE AND PRINCIPLE

Figure 1(a) shows the topology of the conventional SA-PMVM. The machine consists of a stator, a rotor with spoke array permanent magnets (SA-PM), and armature winding. Figure 1(b) shows the topology of the proposed machine. The machine consists of a stator, a rotor with U-type permanent magnets (U-PM), armature windings, and HTS bulks. Compared with conventional machines, the proposed machine introduces alternating flux bridges and uses U-PM instead of SA-PM in the rotor, which provides paths for low pole-pair working harmonics, weakens the magnetic barrier effect, and increases the torque density.

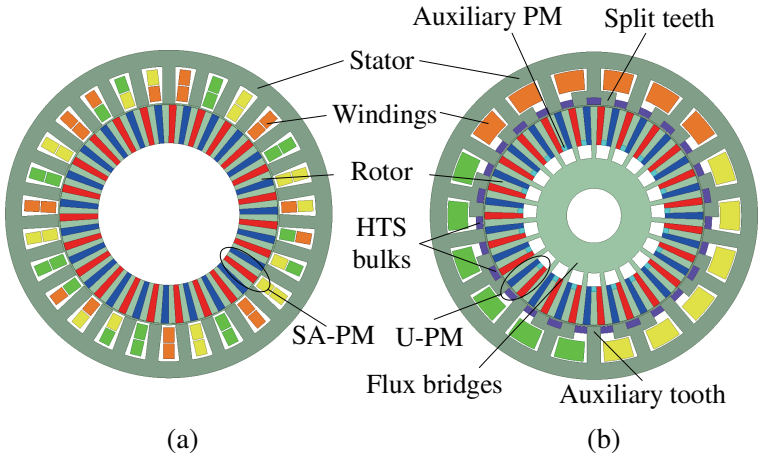

Figure 1. Topology comparison. (a) Conventional machine. (b) Proposed machine.

In addition, the main teeth and auxiliary teeth of the proposed machine are arranged alternately. Each main tooth is divided into two split teeth, and the auxiliary teeth are inserted between the main teeth to modulate the magnetic field together. The armature winding adopts single-layer concentrated winding, and the winding is only wound on the main tooth, which can realize physical isolation between phases, improve the reliability of machine operation, and reduce resistance copper consumption.

However, the introduction of the flux bridge will further increase the magnetic flux leakage and reduce the power factor. Therefore, HTS bulks are introduced to enhance magnetic field modulation. Based on the Meissner effect, HTS has a very low relative permeability, and its magnetoresistance is almost infinite. HTS bulks allow the magnetic flux to pass through the stator and rotor cores as much as possible, thereby shielding the magnetic field and reducing magnetic flux leakage. Figure 2 shows the cross-section of HTS bulk, which is composed of superconducting material, condensate, vacuum chamber, and carbon fiber frame. Cooling is very important for high-temperature superconducting materials, because HTS materials can maintain unique magnetic flux shielding properties only when the temperature is below 77 K [17]. In this study, the condensate is introduced into the superconducting bulk, and the cycle is realized through the cooling tube, reducing the temperature to about 77 K to ensure normal operation.

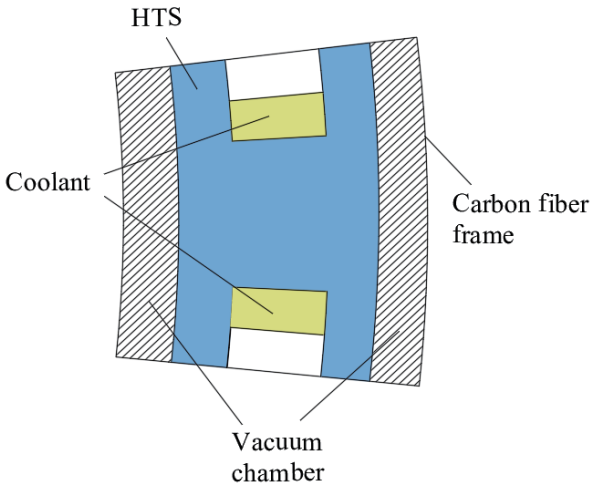

Figure 2. Structure of the proposed HTS bulks.

PMVM based on the magnetic field modulation effect, the number of stator and rotor pole pairs and modulation teeth should meet the following relationship:

$$P_a = Z - P_r \tag{1}$$

where P_a is the number of pole pairs of windings, Z the number of modulation teeth, and P_r the number of pole pairs of PM. P_a, Z, and P_r of the proposed machine are selected as 4, 27, and 23, respectively.

To further illustrate the working principle of the proposed machine, this paper uses the analytical method to obtain the expression of air gap flux density ignoring the high order. The Fourier decomposition of air gap permeance can be expressed as follows:

$$\Lambda(\theta, t) \approx \Lambda_0 + \Lambda_1 \cos(Z\theta_s) \tag{2}$$

where Λ_0 and Λ_1 are the DC and fundamental components of air gap permeance, respectively, and θ_s is the angle between the stator and the A-phase winding axis. The magnetomotive force of PM can be expressed as:

$$F(\theta) \approx F_1 \cos(P_r\theta_r) + F_2 \cos(P_a\theta_r + \theta_{\mathrm{m}}t) \tag{3}$$

where θ_r is the angle between the rotor and the A-phase winding axis, θ_m the relative position of the stator and rotor, F_1 the amplitude of the magnetomotive force harmonic related to the rotor position, and F_2 the oscillating component. From formulas (2) and (3), the air gap flux density can be obtained as follows:

$$\begin{aligned} B_r &= F(\theta)\Lambda(\theta, t) \\ &= B_c \cos(P_r\theta_s + \omega t) + B_m \cos[(Z \mp P_r)\theta_s \pm \omega t] \end{aligned} \tag{4}$$

$$B_c = \Lambda_0 F_1 - \frac{1}{2}\Lambda_1 F_2 \tag{5}$$

$$B_m = \frac{1}{2}\Lambda_1 F_1 - \Lambda_0 F_2 \tag{6}$$

where B_c is a conventional quantity existing in conventional PMSM, and B_m is generated by the flux modulation effect. The existence of the oscillating component will weaken the flux density. The higher the pole ratio is, the lower the B_m and B_c values are, so it is necessary to weaken the magnetic barrier effect at a high ratio.

3. MACHINE OPTIMIZATION DESIGN

Compared with the conventional permanent magnet machine, the electromagnetic performance of the PMVM is more significantly affected by the cogging structure and the size of the permanent magnet. In this paper, the thickness of stator and rotor yoke, the thickness and width of main tooth and split tooth, the width and thickness of permanent magnet, and other key parameters are analyzed and optimized. Figure 3 shows the parameters of the proposed machine. The design of initial values of structural parameters and their reasonable variation range are listed in Table 1.

Table 1. Optimized variable initial and optimized values.

Parameter	Initial	Scope
Stator yoke thickness L_{sy} (mm)	6	$4 \sim 8$
Rotor yoke thickness L_{ry} (mm)	11	$7 \sim 15$
Main tooth thickness L_c (mm)	8.5	$7 \sim 10$
Main tooth width W_c (mm)	5	$3 \sim 7$
Split tooth width W_t (deg)	7	$5 \sim 9$
Slot thickness L_s (mm)	2.6	$2 \sim 3.2$
Slot width W_s (deg)	7	$5 \sim 9$

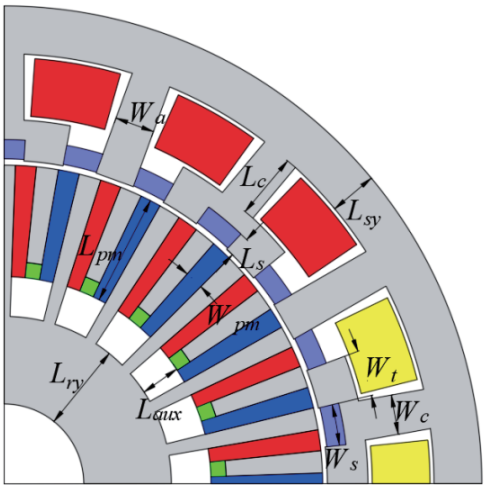

Figure 3. The parameters of the proposed machine.

Figure 4 shows the optimized design flowchart of the proposed machine. In this paper, the electromagnetic torque, torque ripple, and power factor are taken as the optimization objectives. The sensitivity of the parameters was evaluated and layered. According to the sensitivity of the parameters, multi-objective optimization based on GA is carried out. Finally, the optimal structure of the machine is determined.

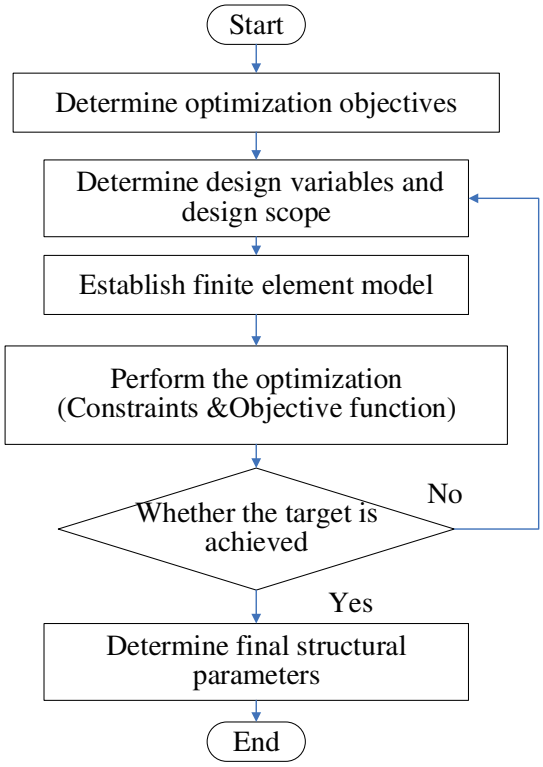

Figure 4. Optimal design flow of the proposed machine.

3.1. Sensitivity Analysis

In order to improve the optimization efficiency, comprehensive sensitivity analysis is used to evaluate and analyze some key parameters. The sensitivity factor $G(x_i)$ and sensitivity coefficient $S(x_i)$ are as follows:

$$\begin{cases} G\left(x_i\right) = \dfrac{V\left(y/x_i\right)}{E\left(y\right)^2} \\ S\left(x_i\right) = \lambda_1 \left|G_e\left(x_i\right)\right| + \lambda_2 \left|G_{ri}\left(x_i\right)\right| + \lambda_3 \left|G_{PF}\left(x_i\right)\right| \end{cases} \tag{7}$$

where x_i is the optimization parameter; $V(y/x_i)$ is the variance of the optimization objective; $E(y)$ is the average value of optimization objectives; $G_{Te}(x_i)$, $G_{Tri}(x_i)$, and $G_{PF}(x_i)$ are the sensitivity factors of electromagnetic torque, torque ripple, and power factor, respectively; λ_1, λ_2, and λ_3 are the weight coefficients of electromagnetic torque, torque ripple, and power factor, respectively, and satisfy $\lambda_1 + \lambda_2 + \lambda_3 = 1$.

The sensitivity analysis results of each parameter are listed in Table 2. It shows that different parameters have different effects on the optimization objectives. Figure 5 shows the histogram for the sensitivity factor in Table 2. The positive sensitivity factor indicates that the optimization objective increases with the increase of optimization variables, while the negative sensitivity factor indicates that the optimization objective decreases with the decrease of optimization variables. The optimization variables with higher absolute values of sensitivity factors mean that the impact of optimization variables on optimization objectives is greater than other variables. It shows that the stator yoke thickness L_{sy}, main tooth thickness L_c, and main tooth width W_c have obvious effects on electromagnetic torque and power factor. The split tooth width W_t and slot width W_s have obvious effects on torque ripple. The auxiliary tooth width W_a has a weak impact on every optimization objective.

Based on the results of the above sensitivity analysis, parameters with sensitivity coefficient less than 0.15 are classified as weak sensitivity parameters [18]. The correlation between the weak sensitivity parameters is weak, and it has little effect on the optimization goal. Therefore, the initial value is directly selected for optimization analysis. Parameters with sensitivity coefficient greater than 0.15 are

Table 2. Sensitivity analysis results of parameters.

Parameter	$G_{Te}(x_i)$	$G_{Tri}(x_i)$	$G_{PF}(x_i)$	$S(x_i)$
L_{sy}	−0.51	0.15	−0.15	0.33
L_{ry}	−0.14	−0.1	−0.004	0.09
L_c	−0.45	0.17	−0.21	0.32
W_c	0.33	−0.19	0.16	0.25
W_t	−0.03	0.01	−0.41	0.13
L_s	−0.1	0.13	0.06	0.09
W_s	0.13	−0.13	0.43	0.22
W_a	0.09	−0.02	−0.01	0.06
L_{pm}	0.19	−0.06	0.18	0.16
W_{pm}	0.11	−0.12	0.21	0.14
L_{aux}	−0.03	−0.08	0.06	0.05

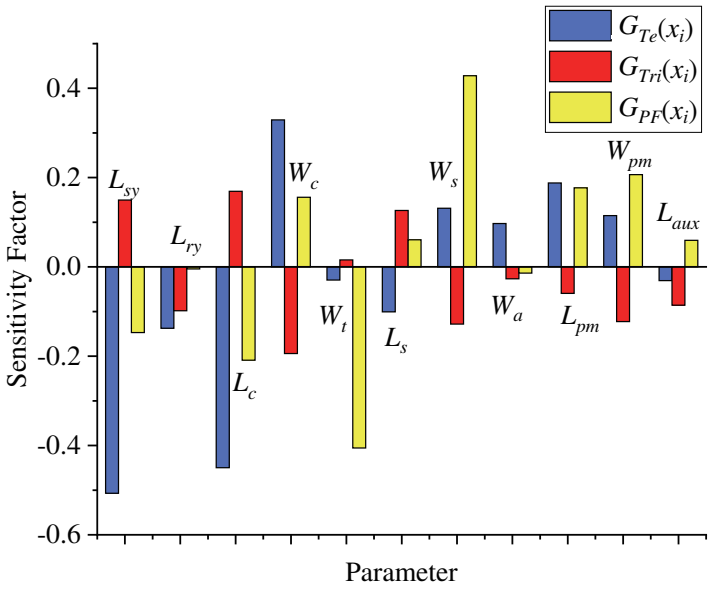

Figure 5. Sensitivity analysis results of parameters.

classified as strong sensitivity parameters. In this paper, stator yoke thickness L_{sy}, main tooth thickness L_c, main tooth width W_c, split tooth width W_t, slot width W_s, PM thickness L_{pm}, and PM width W_{pm} are classified as strong sensitivity parameters, which need to be further analyzed by genetic algorithm.

3.2. Genetic Algorithm Optimization

Based on the above parameter sensitivity analysis, this paper analyzes the model of strong sensitivity parameters and selects large electromagnetic torque, large power factor, and low torque ripple as the optimization objectives of the proposed machine. In order to achieve these three objectives, a multi-objective optimization function $F(x_i)$ is constructed for global optimization:

$$\begin{cases} F(x_i) = \lambda_1 \dfrac{F_{Te}(X)}{T_e} + \lambda_2 \dfrac{T_{ri}}{F_{ri}(X)} + \lambda_3 \dfrac{F_{PF}(X)}{PF} \\ X = [L_{sy}, L_c, W_c, W_t, W_s, L_{pm}, W_{pm}] \end{cases} \tag{8}$$

where X is the space of the optimization variables. T_e, T_{ri}, and PF are the electromagnetic torque, torque ripple, and power factor before optimization, respectively. $F_{Te}(x_i)$, $F_{Tri}(x_i)$, and $F_{PF}(x_i)$ are the electromagnetic torque, torque ripple, and power factor under parameter x_i, respectively.

In this paper, a multi-objective genetic algorithm for global optimization is used. In optimization settings, the initial start population size is set to 20, the pareto-ranking selection set to tournament, the crossover method set to simulated binary, the crossover probability set to 0.5, the mutation type set to self-adaptive, and the mutation rate set to 0.28. In addition, constraints are set to determine whether the optimization process is over. That is, the minimum number of generations is set to 5, and the convergence stability percentage is set to 0.1.

The feasible solution generated in the optimization is shown in Figure 6. To compare with the optimal solution (red dots in the Figure 6), the solution of the Pareto front is selected as the optimal model solution set (blue dots in the Figure 6), and the black dot is used as the optimal compromise solution of the multi-objective optimization result.

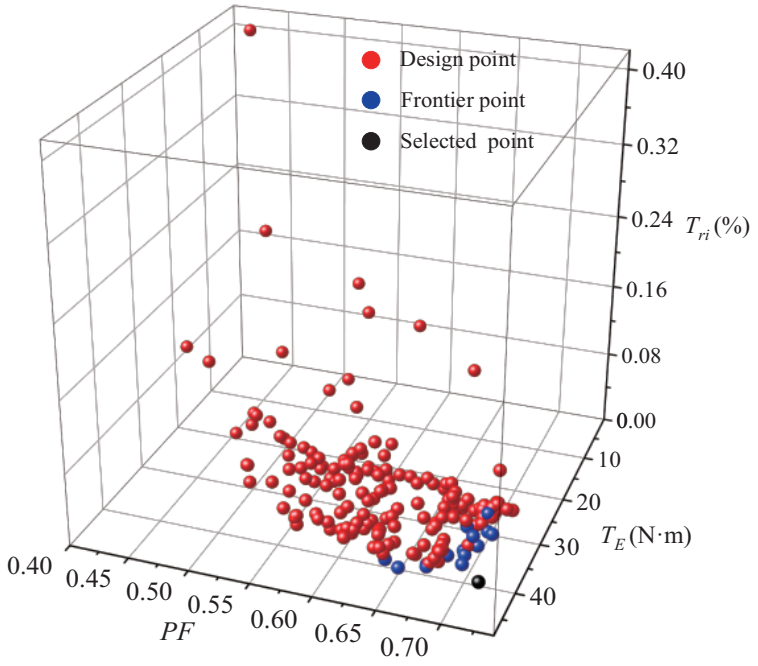

Figure 6. 3D Paetro front.

4. ELECTROMAGNETIC PERFORMANCE COMPARISON

To further study the advantages of the proposed machine, the electromagnetic performances of the conventional machine and the proposed machine are compared by using the finite element analysis. The two machines have the same size structure and permanent magnet consumption. The specific parameters are listed in Table 3.

4.1. Magnetic Flux Density

Figure 7 shows the comparison of the no-load magnetic line. For the conventional machine, the magnetic field of 4 pole pairs bypasses two PMs with reverse excitation, forcing the main magnetic circuit into the air gap, resulting in an increase in the reluctance of the magnetic circuit and a decrease in the main magnetic flux. The proposed machine uses flux bridges in the rotor yoke to provide a magnetic circuit for low order working harmonics, thereby weakening the magnetic barrier effect. In addition, the HTS bulks exert the magnetic resistance characteristic, ensuring that the magnetic line does not pass

Table 3. Structural parameters of the proposed machine.

Parameter	Value
Stator radius (mm)	60
Rotor radius (mm)	40
Axial length (mm)	85
Airgap length (mm)	0.6
Series turns per phase	50
PM material	NdFeB
Iron core material	DW465-50
Rated current (A)	8.8
Rotation speed (rpm)	130

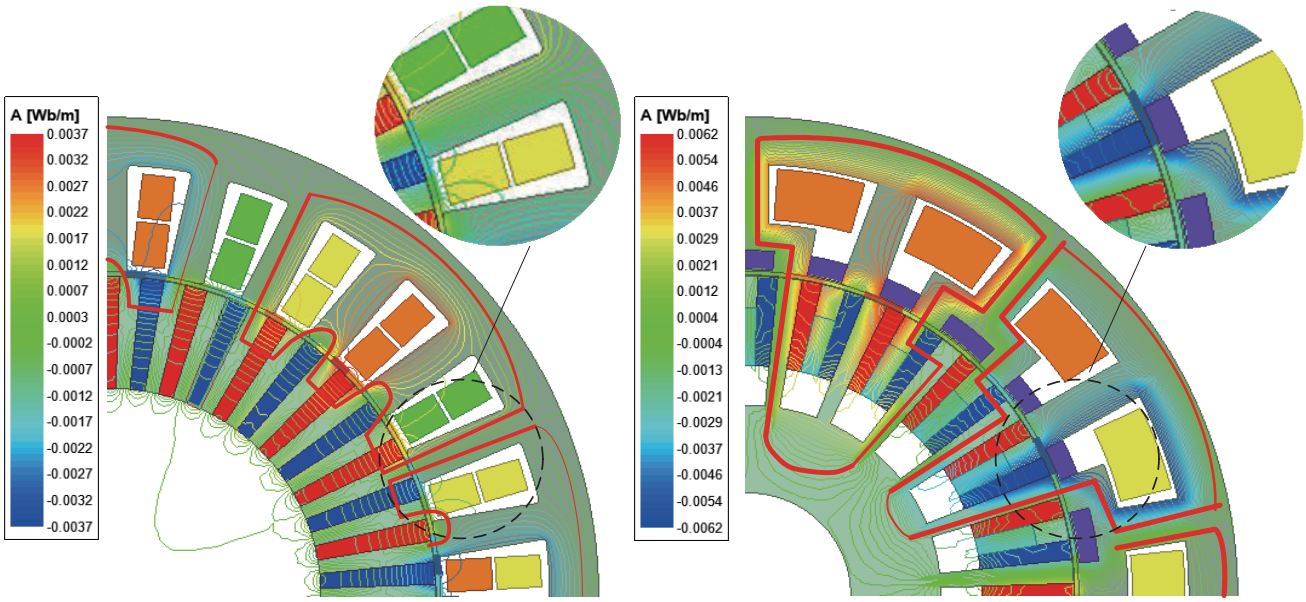

Figure 7. No-load flux line. (a) Conventional machine. (b) Proposed machine.

through the HTS bulks and makes it pass through the iron core as much as possible. HTS bulk not only reduces the flux leakage but also protects the flux linkage.

Figure 8(a) shows the waveform comparison of the radial flux density. It indicates that the radial flux density of the proposed machine has a higher amplitude. Figure 8(b) shows the harmonic spectrum. According to the magnetic field modulation theory, the harmonic components with pole pairs equal to 4, 23, 31, 50, and 58 are working harmonics. The 4th, 31st, and 50th order working harmonics of the proposed machine are larger than those of the conventional machine, which is beneficial to increase the torque. Due to the introduction of flux bridge, the amplitude of low order working harmonics increases greatly. The introduction of HTS bulks and irregular stator teeth increases the amplitude of non-working harmonics, such as 14, 32, 40, 41 harmonics, which will increase the torque ripple, hysteresis loss, and iron loss.

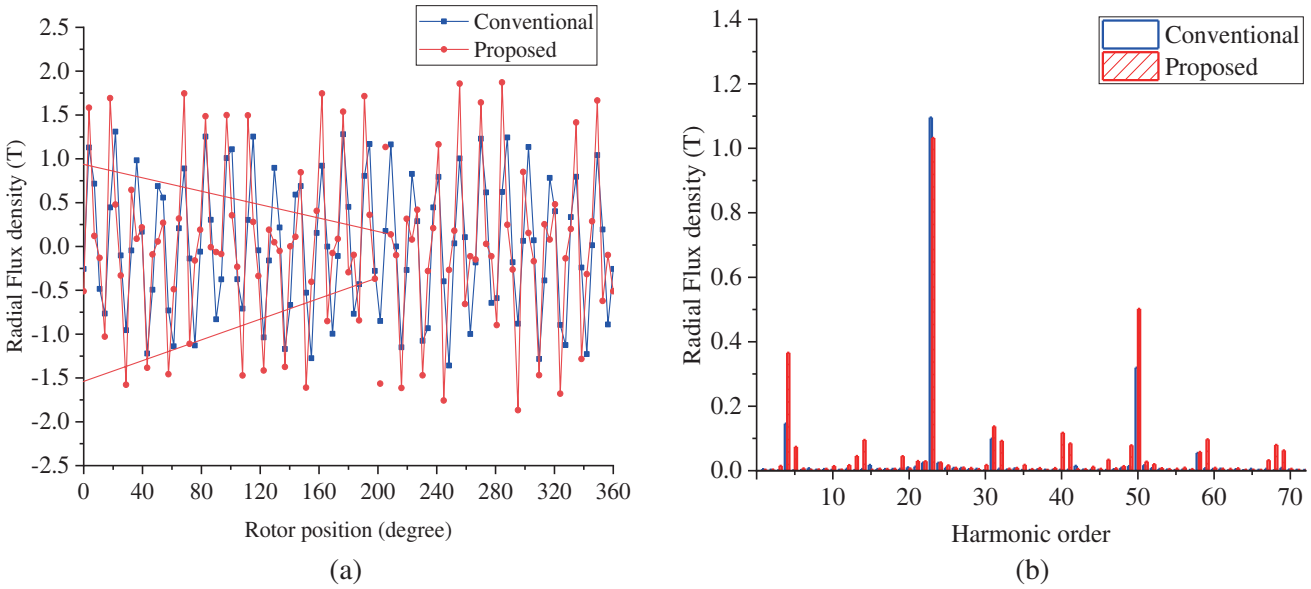

Figure 8. Radial flux density. (a) Waveform. (b) Harmonic spectra.

4.2. No-Load BackEMF

Figure 9(a) shows that the no-load back EMF amplitudes of the proposed machine and the conventional machine are 39 V and 19.4 V, respectively. In spectral analysis, the total harmonic distortion (THD) rate is introduced to analyze the sinusoidal waveform of the back EMF, *THD* as follows:

$$THD = \frac{\sqrt{\sum_{n=2,3,4,\ldots}^{\infty} E_n}}{E_1} \times 100\% \tag{9}$$

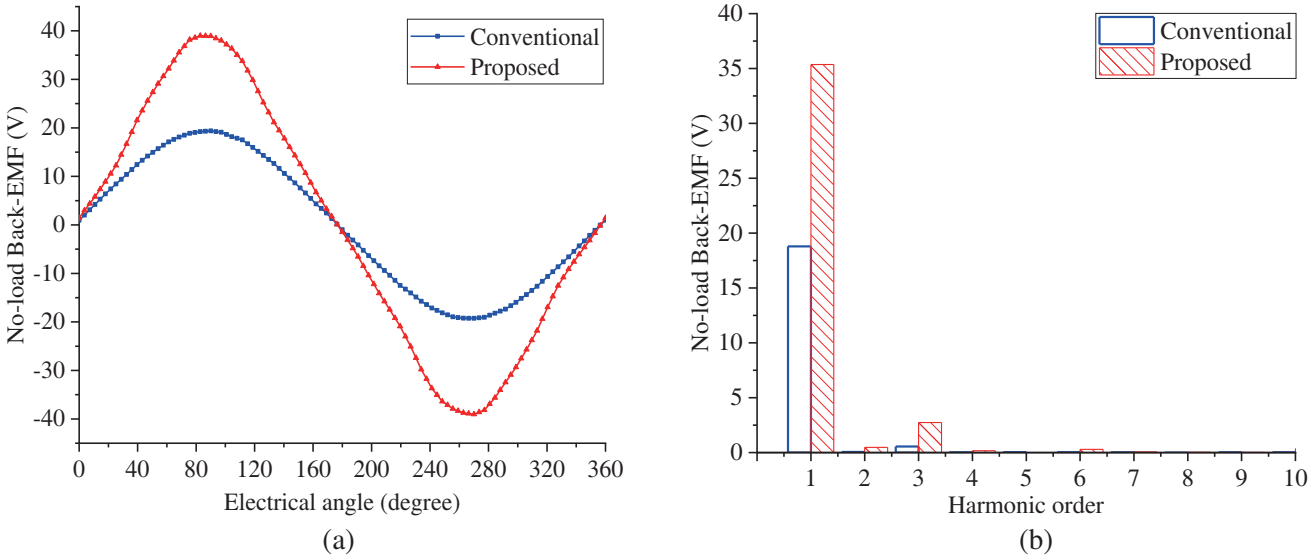

Figure 9. No-load Back EMF. (a) Waveform, (b) Harmonic spectra.

where E_n is the amplitude of the nth harmonic, n the harmonic order, and E_1 the fundamental amplitude.

According to formula (9), the harmonic distortion rate of the proposed machine and the conventional machine can be calculated to be 7.5% and 2.8%, respectively. The largest reason for the increase of back EMF distortion is the unbalance of air gap flux distribution.

4.3. Electromagnetic Torque

According to the Maxwell stress tensor method, the electromagnetic torque is as follows:

$$T_e = \frac{\pi L_e R_g^2}{\mu_0} \sum_{n=1}^{\infty} B_{rn} B_{tn} \cos\left[\theta_{rn}(t) - \theta_{tn}(t)\right] \tag{10}$$

where L_e is the effective axial length; R_g is a circle of radius in the air gap; μ is the permeability of the vacuum; B_{rn} and B_{tn} are the radial and tangential magnetic flux density at the nth harmonic, respectively; θ is the mechanical angle.

The electromagnetic torque waveform is shown in Figure 10. The average electromagnetic torques of the proposed machine and conventional machine are 44.3N·m and 26.2N·m, respectively. The torque density is increased by 69%, and the torque ripple is reduced from 5.6% to 1.7%, indicating that the proposed machine has greater torque transmission capacity and more stable performance.

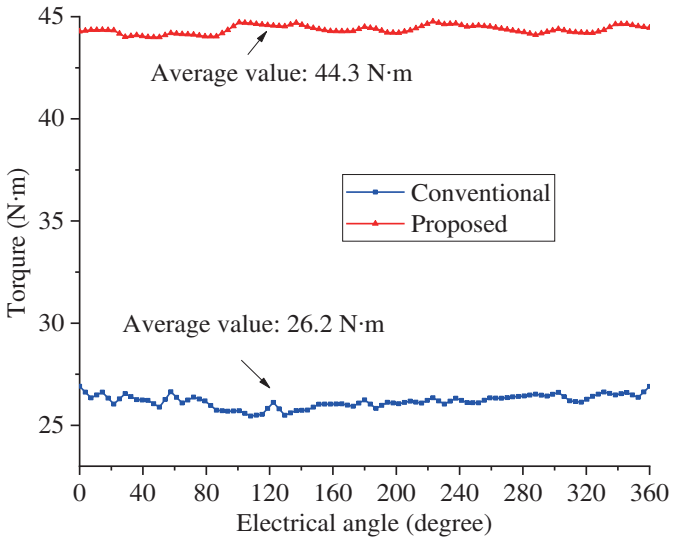

Figure 10. Electromagnetic torque.

4.4. Inductance

Figure 11 shows the inductance waveform of phase A winding. To analyze the reliability of the machine, the coupling coefficient K is defined as follows:

$$K = \frac{L_m}{L_a} \tag{11}$$

where L_m is the maximum effective value of mutual inductance, and L_a is the effective value of self-inductance.

The self-inductance effective value of the A-phase winding of the conventional machine is 3.85 mH, and the maximum mutual inductance is 0.94 mH. The self-inductance effective value of the A-phase winding of the proposed machine is 8.3 mH, and the maximum mutual inductance is 0.12 mH. The calculated coupling coefficients of the conventional machine and the proposed machine are 24.4% and 1.4%, respectively. The coupling effect of the proposed machine is very weak, that is, it has higher reliability.

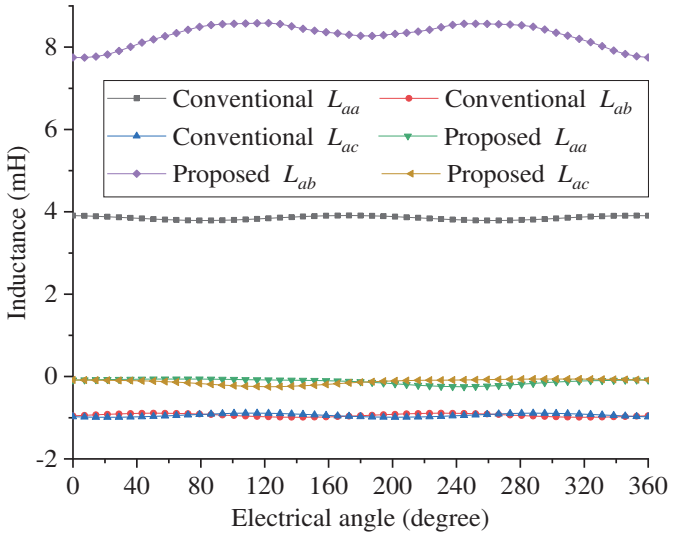

Figure 11. Inductance.

4.5. Power Factor

The machine adopts the control mode of $I_d = 0$ and ignores the phase winding resistance. The power factor PF is as follows:

$$PF = 1/\left(\sqrt{1 + (I_m L_q/\phi_m)^2}\right) \tag{12}$$

whereI_m is the effective value of phase current, L_q the q-axis inductance, and ϕ_m the effective value of no-load PM flux linkage.

Through the analysis of Figure 12, the average q-axis inductances of the conventional machine and proposed machine are 4.8 mH and 8.4 mH, respectively, and the effective value of the no-load PM flux linkage is 0.042 Wb and 0.078 Wb. The magnetic flux leakage shielding effect of the HTS bulks reduces the magnetic flux leakage between teeth, which effectively improves the no-load flux linkage. According

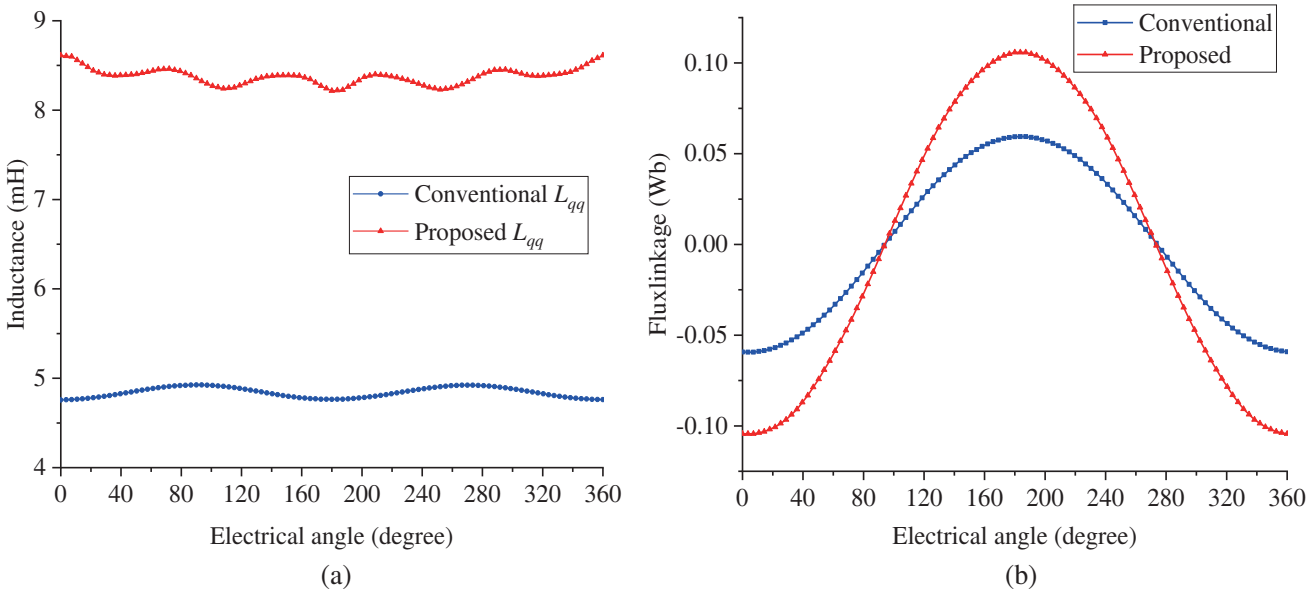

Figure 12. (a) q-axis inductance. (b) Flux linkage.

to formula (12), the power factors of the conventional machine and proposed machine are 0.7 and 0.73, respectively. This indicates a slight improvement in the power factor of the proposed machine.

4.6. Loss and efficiency

Figure 13, Figure 14, and Figure 15 are the copper loss waveform, core loss waveform, and eddy current loss waveform of the machine model, respectively. According to Figure 13, the copper loss of the proposed machine is 62.67 W, which is 15.74 W lower than that of the conventional machine. It can be seen from Figure 14 that the core losses of the proposed machine and conventional machine are 7.58 W and 2.47 W, respectively. In addition, Figure 15 shows that the eddy current losses of the proposed machine and conventional machine are 34.2 W and 11.13 W, respectively. Various losses, output powers, and efficiencies are listed in Table 4.

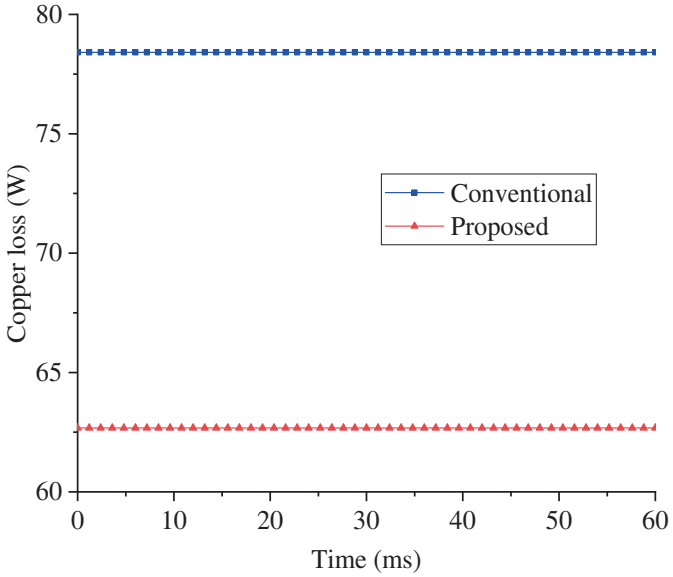

Figure 13. Copper loss.

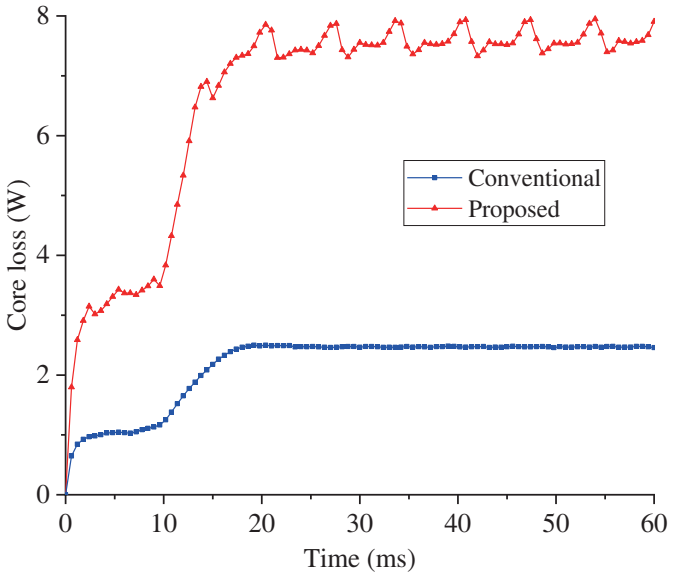

Figure 14. Core loss.

Figure 16 shows the total loss cloud diagram. The loss is mainly distributed on the machine winding and permanent magnet. From Figure 16 and Table 4, the resistance copper loss of the proposed machine is smaller, and the main reason is that the machine adopts a single-layer concentrated winding with a

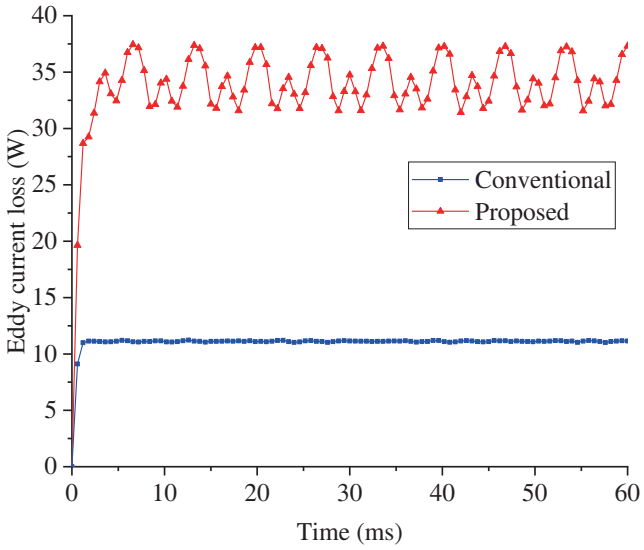

Figure 15. Eddy current loss of permanent magnet.

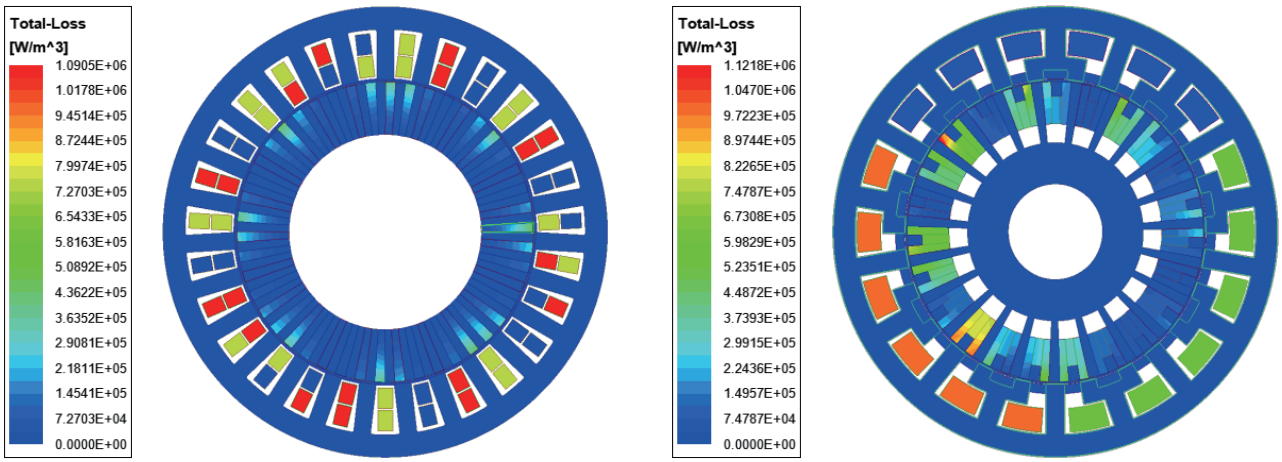

Figure 16. Total loss cloud diagram. (a) Conventional machine. (b) Proposed machine.

Table 4. Various losses, output power and efficiency.

Parameter	Conventional	Proposed
Copper loss (W)	78.41	62.67
Core loss (W)	2.47	7.58
Eddy current loss (W)	11.13	34.2
Total loss (W)	92.01	104.45
Output power (W)	357.9	605.1
Efficiency	79.6%	85.3%

span of 1, and the winding pitch is smaller than that of the conventional machine, which can reduce the resistance copper loss and improve the efficiency of the machine. The proposed machine has more core loss, which is mainly caused by the complex rotor structure using more silicon steel. The eddy current loss of the proposed machine is mainly caused by the PM, and this loss is larger than that of the conventional machine. The main reason is that the proposed machine contains more non-working harmonics whose harmonic speed is not synchronized with the rotor PM.

5. CONCLUSION

In this paper, a U-PM vernier machine with HTS bulks has been proposed and analyzed. In this study, the finite element method was used to establish the machine parameter model. The parameters are layered by comprehensive sensitivity analysis, and the key parameters are optimized by genetic algorithm. Finally, through finite element verification, the proposed machine has better electromagnetic performance. The contributions of this study are summarized as follows.

(1). Compared with the conventional machine, the proposed machine can weaken the magnetic barrier effect. By introducing flux bridges and U-PMs into the rotor, the flux path is provided for the low-pole-pair working harmonics. The fourth order working harmonic amplitude of the proposed machine is twice of that of the conventional machine. The average electromagnetic torque of the proposed machine is 69% higher than the conventional machine, and the torque ripple is reduced to 1.7%.

(2). Compared with conventional machine, the outer stator of the machine model adopts the structure of alternating arrangement of main teeth and auxiliary teeth, which can improve the reliability. The inductance coupling coefficient of the proposed machine is 1.4%, which is much smaller than that of the conventional machine. The use of high temperature superconducting bulk materials reduces the magnetic flux leakage between teeth and optimizes the harmonic distribution in the air gap. The power factor of the proposed machine is increased to 0.73.

(3). Compared with the conventional machine, the output power of the proposed machine is increased by 69% and the efficiency increased by 5.7%. Therefore, the proposed machine has better performance.

REFERENCES

1. Li, X., X. Wang and Y. Wang, "Design and analysis of a new HTS linear flux-controllable doubly salient machine," *IEEE Trans. Appl. Supercond.*, Vol. 29, No. 5, 1–5, Aug. 2019.
2. Li, W., T. W. Ching, K. T. Chau, and C. H. T. Lee, "A superconducting vernier motor for electric ship propulsion," *IEEE Trans. Appl. Supercond.*, Vol. 28, No. 3, 1–6, Apr. 2018.
3. Köster, R. and A. Binder, "Multi-objective optimization of a direct-drive wind turbine generator with HTS excitation winding," *IEEE Trans. Appl. Supercond*, Vol. 32, No. 4, 1–8, Jun. 2022.
4. Li, X., S. Liu, and Y. Wang, "Design and analysis of a stator HTS field-modulated machine for direct-drive applications," *IEEE Trans. Appl. Supercond.*, Vol. 27, No. 4, 1–5, Jun. 2017.
5. Wu, D., Z. Xiang, X. Zhu, L. Quan, M. Jiang, and Y. Liu, "Optimization design of power factor for an in-wheel vernier PM machine from the perspective of air-gap harmonic modulation," *IEEE Trans. Ind. Electron.*, Vol. 68, No. 10, 9265–9276, Oct. 2021.
6. Xie, K., D. Li, R. Qu, and Y. Gao, "A novel permanent magnet vernier machine with Halbach array magnets in stator slot opening," *IEEE Trans. Magn.*, Vol. 53, No. 6, 1–5, Jun. 2017.
7. Xu, L., W. Zhao, G. Liu, and C. Song, "Design optimization of a Spoke-type permanent-magnet vernier machine for torque density and power factor improvement," *IEEE Trans. Veh. Technol.*, Vol. 68, No. 4, 3446–3456, Apr. 2019.
8. Zhang, Y., D. Li, P. Yan, X. Ren, R. Qu, and J. Ma, "A high torque density claw-pole permanent-magnets vernier machine," *IEEE J. Emerg. Sel. Top. Power Electron.*, Vol. 10, No. 2, 1756–1765, Apr. 2022.

9. Ren, X., D. Li, R. Qu, Z. Yu, and Y. Gao, "Investigation of spoke array permanent magnet vernier machine with alternate flux bridges," *IEEE Trans. Energy Convers.,* Vol. 33, No. 4, 2112–2121, Dec. 2018.
10. Baloch, N., S. Khaliq, and B.-I. Kwon, "A high force density HTS tubular vernier machine," *IEEE Trans. Magn.*, Vol. 53, No. 11, 1–5, Nov. 2017.
11. Ardestani, M., N. Arish, and H. Yaghobi, "A new HTS dual stator linear permanent magnet vernier machine with Halbach array for wave energy conversion," *Phys. C Supercond.*, Vol. 569, Feb. 2020.
12. Jing, L., W. Tang, W. Liu, Y. Rao, C. Tan, and R. Qu, "A double-stator single-rotor magnetic field modulated motor with HTS bulks," *IEEE Trans. Appl. Supercond.*, Vol. 32, No. 6, 1–5, Sep. 2022.
13. L. Li, G. Zhu, X. Liu, H. Chen, W. Jiang, and M. Xue, "Design and optimization of a novel HTS flux-modulated linear motor using Halbach permanent magnet arrays," *IEEE Trans. Appl. Supercond.*, Vol. 31, No. 8, 1–4, Nov. 2021.
14. Guo, Y., J. Si, C. Gao, H. Feng, and C. Gan, "Improved Fuzzy-Based Taguchi Method for Multi-Objective Optimization of Direct-Drive Permanent Magnet Synchronous Motors," *IEEE Trans. Magn.*, Vol. 55, No. 6, 1–4, Jun. 2019.
15. Zhao, W., A. Ma, J. Ji, X. Chen, and T. Yao, "Multiobjective optimization of a double-side linear vernier PM motor using response surface method and differential evolution," *IEEE Trans. Ind. Electron.*, Vol. 67, No. 1, 80–90, Jan. 2020.
16. Jia, S., K. Yan, D. Liang, R. Qu, J. Liu, and J. He, "A novel DC-biased current dual pm vernier machine," *IEEE Trans. Ind. Appl.,* Vol. 57, No. 5, 4595–4605, Sept.–Oct. 2021.
17. Arish, N., F. Marignetti, and M. Yazdani-Asrami, "Comparative study of a new structure of HTS-bulk axial flux-switching machine," *Phys. C Supercond.*, Vol. 584, 2021.
18. Xu, L., W. Wu, W. Zhao, G. Liu, and S. Niu, "Robust design and optimization for a permanent magnet vernier machine with hybrid stator," *IEEE Trans. Energy Convers.*, Vol. 35, No. 4, 2086–2094, Dec. 2020.